RSC Applied Interfaces

ROYAL SOCIETY OF CHEMISTRY

PAPER

View Article Online
View Journal | View Issue

Cite this: *RSC Appl. Interfaces*, 2026, **3**, 135

Bio-nanocomposite Eri silk fibroin/zinc oxide for antibacterial and anticancer applications

Bidhu Bhushan Brahma, [a] Mousumi Narzary, [a] Arijit Mondal, [b] Debjani Das,[c] V. G. M. Naidu,[b] Sandeep Das,[c] Pranjal Kalita [d] and Manasi Buzar Baruah *[a]

The increasing prevalence of multidrug-resistant (MDR) bacteria and aggressive breast cancers such as triple-negative breast cancer (TNBC) poses a significant challenge to current therapeutic strategies, necessitating the development of novel, biocompatible and multifunctional materials. In this study, a bio-nanocomposite matrix of Eri silk fibroin–zinc oxide (ESF@ZnO) has been successfully synthesized and characterized to explore its potential for antibacterial and anticancer applications. XRD, FTIR, UV-vis, FESEM and TEM demonstrated the successful integration of ZnO within the ESF matrix. FESEM of the ESF@ZnO composite revealed a heterogeneous surface morphology with ZnO nanoflakes embedded within the silk fibroin matrix. TEM further confirmed the incorporation of crystalline ZnO structures into the amorphous network, while SAED patterns displayed both sharp diffraction rings from ZnO and diffuse halos from ESF, validating the formation of a hybrid organic–inorganic nanocomposite. The antibacterial activity of ESF@ZnO was evaluated against *Escherichia coli* and *Bacillus subtilis* with an inhibition zone of 14.8 ± 0.15 mm and 13.2 ± 0.14 mm, respectively. Furthermore, ESF@ZnO exhibited significant anticancer activity against 4T1 (mouse breast cancer) and MDA-MB-231 (human triple-negative breast cancer) cell lines, with IC_{50} values of 84.06 ± 21.13 and 29.76 ± 13.46 μg mL^{-1}, respectively. A dose-dependent reduction in cell viability and statistically significant cytotoxic effects ($p < 0.001$) were observed, confirming its effectiveness in inducing cancer cell death. These results highlight ESF@ZnO as a promising bio-nanocomposite for future antibacterial and anticancer applications.

Received 10th September 2025,
Accepted 13th November 2025

DOI: 10.1039/d5lf00271k

rsc.li/RSCApplInter

1. Introduction

The rapid rise of antimicrobial resistance (AMR) or multidrug-resistance (MDR) and aggressive cancers such as triple-negative breast cancer (TNBC) poses serious global health challenges.[1,2] MDR pathogens such as *Escherichia coli* (*E. coli*) are increasingly resistant to conventional antibiotics due to overuse, genetic mutations, and horizontal gene transfer (HGT).[3] According to the World Health Organization (WHO), antimicrobial resistance (AMR) directly caused 1.27 million deaths in 2019, with projections indicating up to 10 million annual fatalities by 2050 if left unaddressed.[4,5] Unlike MDR bacteria, Gram-positive bacteria like *Bacillus subtilis* do not acquire resistance genes as readily through HGT and are also responsible for causing many diseases such as meningitis, septicaemia, pneumonia, endocarditis, wound infection and intraocular inflammation.[6] Simultaneously, cancer remains a leading cause of mortality worldwide, responsible for nearly 10 million deaths in 2020.[7] Among various types, breast cancer accounted for 2.26 million cases that year.[7] Breast cancer is highly heterogeneous, classified into different subtypes such as hormone receptor-positive (HR+), HER2-positive, and triple-negative breast cancer (TNBC).[8] Among these, TNBC is the most aggressive and difficult to treat, as it lacks the expression of hormone receptors (estrogen and progesterone) and HER2, as a result TNBC does not respond to hormone therapies or HER2-targeted treatments, making it highly challenging to treat.[9] 4T1 and MDA-MB-231 cell lines are widely used models of TNBC due to their invasiveness, chemoresistance and metastatic potential.[10]

In response to the risks posed by bacterial infections and cancer, the development of antibacterial and anticancer materials has arisen as an important strategy. Materials like AgNPs, TiO_2, CuO and ZnO exhibit both antibacterial and anticancer activities.[11–14] Among these, ZnO nanoparticles (ZnO NPs) stand out for their ability to generate reactive oxygen species (ROS), which play a key role in antimicrobial and

[a] *Department of Physics, Central Institute of Technology Kokrajhar (Deemed to be University, Ministry of Education, Govt. of India), Assam-783370, India. E-mail: mbbaruah@cit.ac.in*
[b] *Department of Pharmacology & Toxicology, NIPER Guwahati, Assam-781101, India*
[c] *Department of Biotechnology, Bodoland University, Kokrajhar, Assam-783370, India*
[d] *Department of Chemistry, Central Institute of Technology Kokrajhar (Deemed to be University, Ministry of Education, Govt. of India), Assam-783370, India*

anticancer mechanisms.[15,16] According to reports, ZnO NPs were effective at killing Gram negative bacteria as well as Gram-positive bacteria.[17] ZnO NPs have also demonstrated dose-dependent cytotoxicity against cancer cells, promoting apoptosis while exhibiting limited toxicity toward normal cells.[18] Despite these benefits, ZnO NPs face challenges such as poor biocompatibility, cytotoxicity toward normal cells, and a strong tendency to agglomerate, which reduces stability and functional efficiency.[19,20] To address these challenges, efforts have been directed towards the development of ZnO-based composites incorporating natural polymers which make the materials biocompatible.[21] Biocompatible supports such as chitosan, polypyrrole, and silk fibroin have shown promise in enhancing stability, reducing toxicity, and enabling targeted applications.[22–25] However, the challenges related to this area are functionalization and impregnation of natural polymers with nanoparticles for different applications, which must be overcome.[26,27]

Eri silk is a natural polymer which is extracted from the cocoon of Eri silkworm (*Samia ricini*). It consists of two types of protein which are fibroin and sericin. Fibroin is the main structural protein composed of repeated amino acid blocks ended with C and N units which provide the strength to the silk whereas sericin binds the fibroin together with its gluey nature.[28] Recent research has demonstrated the potential of *Bombyx mori* silk to serve as a template for the synthesis of nanoparticles.[29,30] However, ESF remains underexplored despite its distinct physical and chemical properties. The utilization of silk fibroin as a matrix for immobilizing ZnO NPs offers a stable and biocompatible solution, effectively tackling issues related to nanoparticle aggregation.[31] Here, we present a novel bio-nanocomposite of ESF and ZnO NPs, where ZnO NPs are incorporated into the ESF matrix using a simple *in situ* blending approach. This approach not only improves the biocompatibility of the nanocomposite but also showcases good antibacterial and anticancer capabilities. This innovative combination offers a potential hybrid organic–inorganic bio-nanocomposite for advanced applications in biomedical fields.

2. Experimental sections

2.1. Materials

The cocoons of Eri silkworm (*Philosamia ricini*) were obtained from Directorate of Sericulture, Kokrajhar, Assam, India. Sodium carbonate (Na_2CO_3) with a purity of over 99.5% and calcium nitrate ($Ca(NO_3)_2$) with a purity of over 98% were purchased from MERCK. Ethanol (reagent grade >99.9%) was purchased from CSS. Dialysis membrane-70 having a molecular weight cutoff (MWCO) of 12–14 kDa was purchased from Himedia. Zinc acetate ($ZnC_4H_6O_4$) with a purity of over 98% and potassium hydroxide (KOH) with a purity of over 84% were purchased from MERCK. Glutaraldehyde was purchased from MERCK with a purity of 23–27%. Two pathogenic microbes (one Gram positive and another Gram negative) *viz.*, *Escherichia coli* (MTCC 443) and *Bacillus subtilis* (MTCC 441) were purchased from Microbial Type Culture Collection and Gene Bank (MTCC). The BALB/c strain-derived mouse breast cancer cell line 4T1 and the human triple-negative breast cancer cell line MDA-MB-231 were obtained from the American Type Culture Collection (ATCC, Manassas, VA, USA), with catalog numbers ATCC® CRL-2539™ and ATCC® HTB-26™, respectively. DMEM medium, RPMI-1640 medium, certified foetal bovine serum (FBS), 0.25% trypsin EDTA and penicillin–streptomycin antibiotic solution were purchased from Gibco. MTT (3-[4,5-dimethylthiazol-2-yl]-2,5-diphenyltetrazolium bromide) was purchased from Sigma. All other cell culture consumables and chemicals were procured from Tarsons.

2.2. Preparation of Eri silk fibroin solution

Initially, the Eri silk cocoons were cut into smaller fragments, and subsequently subjected to a process called degumming, which involved boiling them in a 0.02 M solution of Na_2CO_3 for a duration of 1 hour in order to eliminate the sericin component.[32] Following the removal of sericin, the degummed silk underwent three thorough washes with deionized water and was subsequently placed in an oven for a night.[33] The extraction of ESF was performed using the dissolution method. The degummed Eri silk was dissolved in a solvent mixture of calcium nitrate, ethanol and water in a ratio of 1 : 4 : 1.5, maintaining a concentration of 2.5 w/v% and heated at 120 °C for 8 to 9 hours. Afterwards, the silk solution underwent dialysis using a dialysis membrane against distilled water for a duration of 3 days, resulting in the extraction of ESF. The distilled water was replaced every 24 hours in order to eliminate the salts. Subsequently, the ESF solution was centrifuged for 10 minutes to eliminate any remaining undissolved silk residue. The ESF solution obtained was stored at a temperature of 4 °C for future use. The same has been illustrated in Scheme 1.

2.3. Preparation of ZnO NPs

To prepare ZnO NPs, zinc acetate was taken as a precursor. A solution of zinc acetate was prepared with a (w/v%) of 2% and then it was stirred for 30 min at room temperature. After that, KOH was added into the solution. A slightly white milky solution was observed. The solution was continuously stirred for about 1 hour at room temperature. After formation of the precipitate, it was washed several times with DI water. Then it was kept in the oven overnight. The complete step by step process is illustrated in Scheme 2.

2.4. Preparation of ESF@ZnO NPs

To prepare the bio-nanocomposite of ESF and ZnO NPs, prepared ZnO NPs were added into 3% (w/v%) ESF solution. The solution was then sonicated for 30 min. After that, glutaraldehyde was added into the solution for the proper linking of ZnO NPs and ESF. Then the solution was kept overnight at room temperature. After GA crosslinking, samples were thoroughly rinsed with ethanol followed by multiple distilled-water washes to remove unreacted GA and

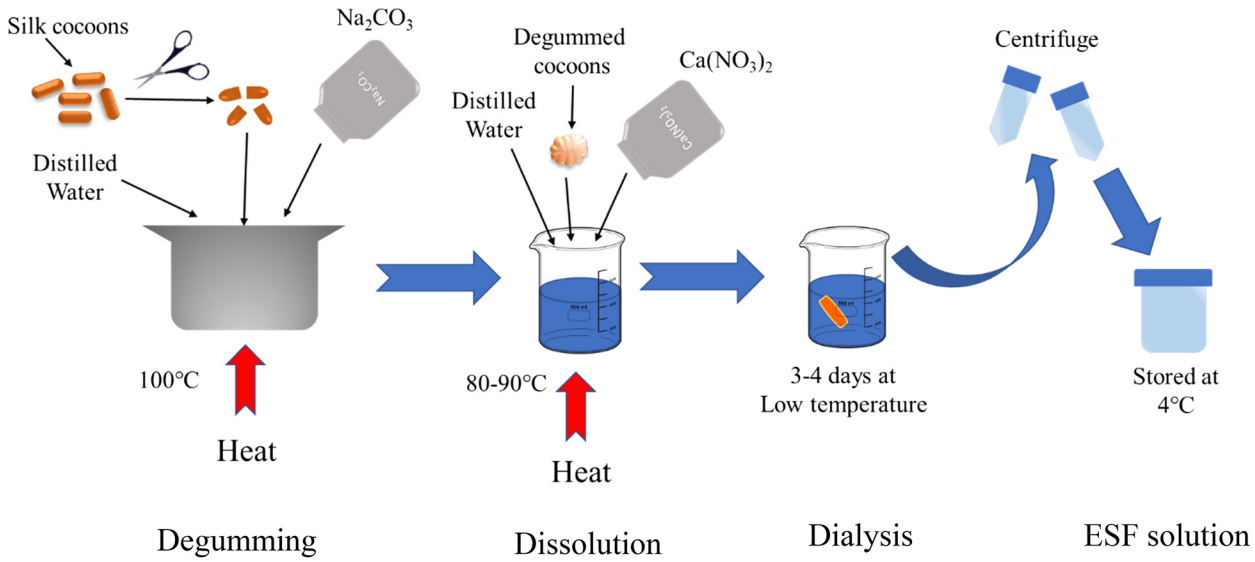

Scheme 1 Preparation of ESF.

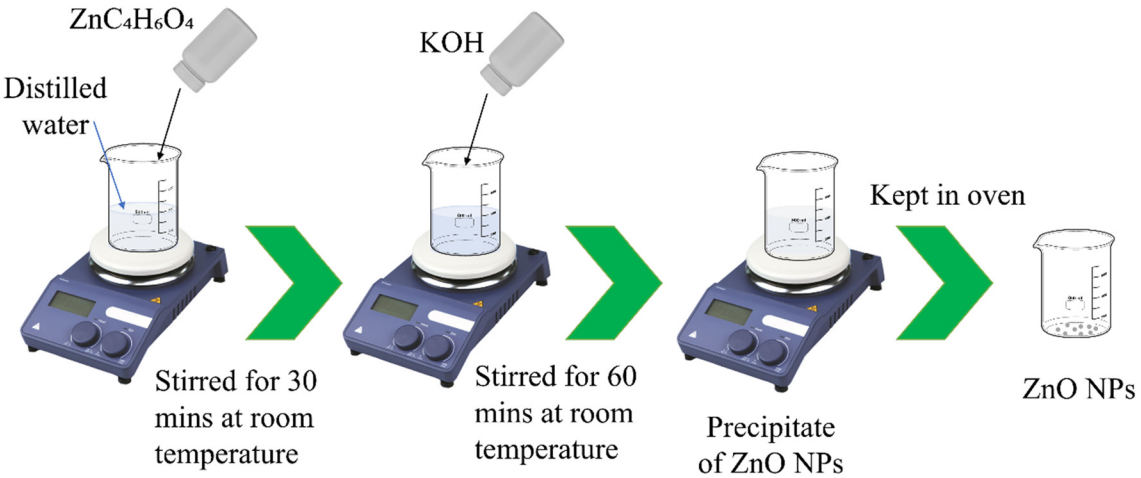

Scheme 2 Preparation of ZnO NPs.

small oligomers. This step was performed immediately after crosslinking to minimize residual aldehyde content. After this, the solution was kept in the oven for drying and then kept in a sample container for further use. The complete step by step process is illustrated in Scheme 3.

2.5. Antibacterial activity

The antibacterial activity test was conducted using the method developed by Priyanka P. Patil, with slight adjustments. Initially, pathogenic bacteria that were 24 hours old were introduced into Mueller Hinton broth and then placed in an incubator at a temperature of 37 °C for 24 hours. Following a 24-hour incubation period, both the bacterial strains, *Escherichia coli* and *Bacillus subtilis*, were applied onto Mueller Hinton Agar media using a sterilized glass spreader. Subsequently, discs containing various samples were positioned on the same plate and kept at a temperature of 37 °C for another 24 hours. The diameter of the zone of inhibition was determined for the sample that exhibited a positive result. The test was repeated three times.

2.6. Anticancer activity

2.6.1. Cell culture. The cell lines used in this study are established and commercially available through ATCC and do not require further Institutional Review Board (IRB) or Institutional Animal Ethics Committee (IAEC) approval. No primary human or animal subjects were used. Hence, informed consent and additional ethical clearance were not applicable. 4T1 and MDA-MB-231 cells were maintained in Dulbecco's modified Eagle medium (DMEM) and Roswell

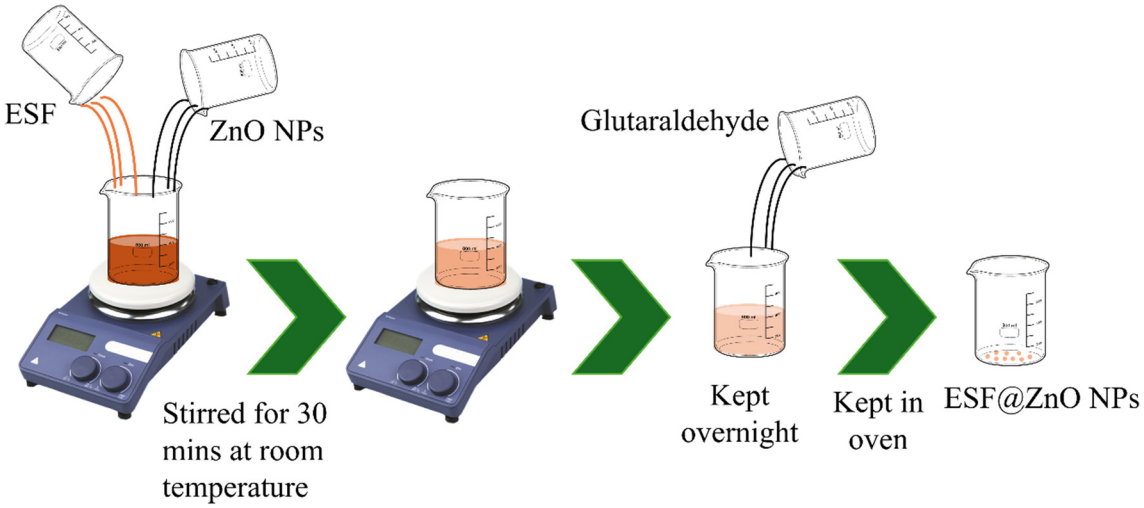

Scheme 3 Preparation of ESF@ZnO NPs.

Park Memorial Institute medium (RPMI-1640) respectively enriched with 10% fetal bovine serum (FBS) and 1% penicillin/streptomycin at 37 °C in a humidified atmosphere with 5% CO_2 supplied incubator.[34,35] The cell lines were sub-cultured by enzymatic digestion with 0.25% trypsin–0.53 mM EDTA when they became approximately 70–80% confluent.[36]

2.6.2. Cell viability. The cell viability was determined by the MTT assay according to Fotakis and Timbrell (2006) with slight modifications. MTT (3-[4,5-dimethylthiazol-2-yl]-2,5-diphenyltetrazolium bromide) is a water-soluble tetrazolium salt that is converted to an insoluble purple formazan by cleavage of the tetrazolium ring by succinate dehydrogenase in the mitochondria. The formazan product is deposited within healthy cells as it cannot penetrate through the cell membrane.[37] 4T1 cells were seeded at a density of 6.5×10^3 in 100 μL RPMI-1640 medium and were plated in 96 well plates. MDA-MB-231 cells were seeded at a density of 6×10^3 in 100 μL DMEM medium and were plated in 96 well plates. Cells were allowed to attach for 24 hours in a CO_2 incubator. Then cells were treated with different concentrations of the compounds in FBS free medium for 24 hours. Following the treatment, 100 μL of MTT (0.5 mg ml^{-1}) was prepared in FBS-free medium and incubated at 37 °C for 4 hours, after removing the medium with compounds. Subsequently, the MTT-containing medium was removed and the resulting purple formazan crystals were dissolved in 100 μL of DMSO. The absorbance was then measured at 570 nm using a Flex Station 3 Multi-mode Microplate reader (Molecular Devices, USA).

3. Material characterization

The X-ray diffraction patterns (XRD) were obtained using an EMPYREAN diffractometer apparatus, with a CuKα incident beam (λ = 1.54 Å), in the 2θ range of 10–80 degrees, with a step size of 0.02 degrees. The Fourier transform infrared (FTIR) spectroscopy technique was employed using a SHIMADZU FTIR 8201 instrument, using the KBr pallet method, in the wavelength range of 4000 to 500 cm^{-1} to identify functional groups and molecular interactions. A UV-vis spectrophotometer (SHIMADZU, UV-2600) covering the wavelength range of 200–800 nm was used to observe the absorbance spectra of the samples. The surface morphology of the sample was studied using a Gemini 500 FE-SEM. HRTEM and SAED were conducted using a JOEL, JEM-2100 PLUS (HR) instrument.

4. Results and discussion

4.1. Powder X-ray diffraction (PXRD) study

Powder X-ray diffraction (PXRD) was conducted to analyse the crystallographic structure of ESF, ZnO NPs, and ESF@ZnO NPs. The objective of this study was to better understand and confirm the structural incorporation of ZnO NPs into the ESF matrix and to identify any alterations in the crystallographic characteristics caused by this amalgamation. Fig. 1 shows the PXRD for (a) ESF, (b) ZnO NPs and (c) ESF@ZnO NPs. Fig. 1(a) reveals that the ESF exhibits peaks (2θ) at 16.7° and 20.2°, indicating a corresponding spacing (d) of 5.30 and 4.50 Å, respectively. These findings suggest the presence of an alpha helix structure. The peaks seen at 2θ values of 24° and 30°, with corresponding interplanar spacings (d) of 3.771 and 3.13 Å, indicate the presence of a beta sheet structure.[38] Fig. 1(b) shows peaks (2θ) at 31.8°, 34.4°, 36.3°, and 47.5°, corresponding to miller indices (100), (002), (101), and (102), indicating the formation of ZnO NPs.[39] Fig. 1(c) shows the peaks (2θ) of ESF@ZnO NPs. It can be clearly observed that an amorphous region has been formed with the crystalline regions of ZnO NPs which confirms the formation of the bio-nanocomposite. The average crystallite size of ESF@ZnO NPs was calculated using the Debye–Scherrer's equation[40] and is illustrated in eqn (1),

$$D = \frac{K\lambda}{\beta \cos\theta} \quad (1)$$

where K is the Scherrer constant (K = 0.94), λ is the X-ray wavelength (λ = 0.154 nm), β is full width at half maximum

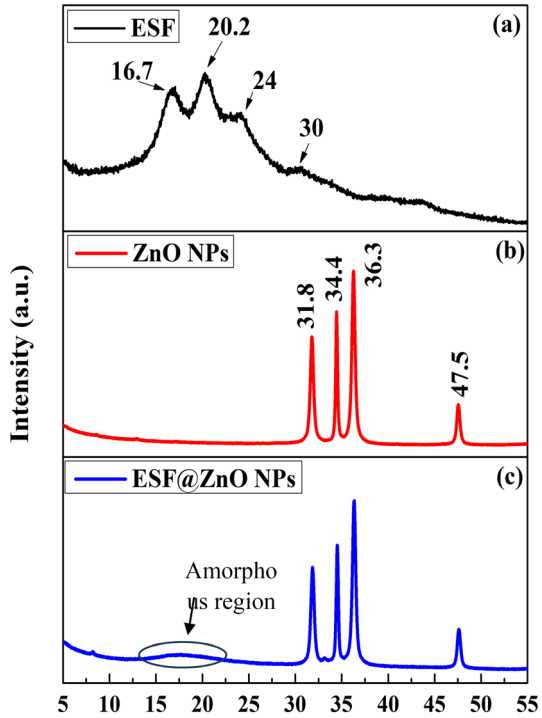

Fig. 1 PXRD of (a) ESF, (b) ZnO NPs and (c) ESF@ZnO NPs.

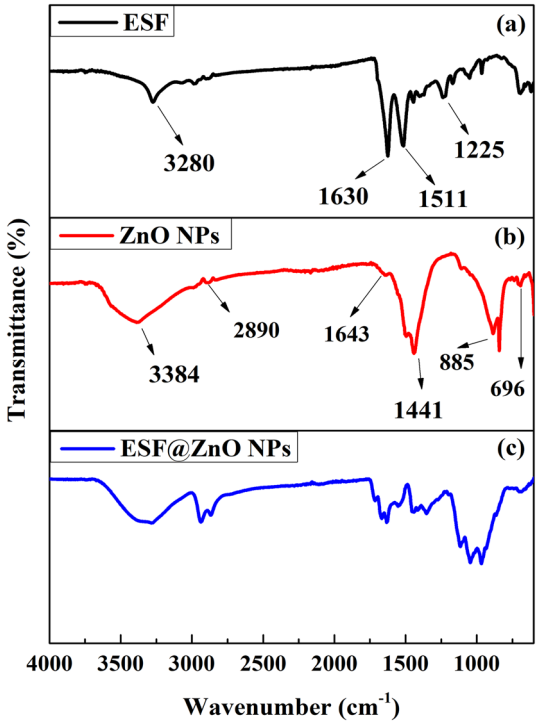

Fig. 2 FTIR of (a) ESF, (b) ZnO NPs and (c) ESF@ZnO NPs.

(FWHM) and θ is the diffraction angle. The average crystallite size of ESF@ZnO NPs was found to be around 27 nm. The crystallinity of pure ZnO NPs was 83% but the crystallinity of ESF@ZnO NPs was found to be 80%. The observed reduction in crystallinity reflects the effective embedding of ZnO NPs into the ESF matrix. The reduced crystallinity also suggests an increase in surface defect sites that can enhance reactive oxygen species (ROS) generation which is one of the primary mechanisms responsible for the observed antibacterial and anticancer activities.[41,42] Such defect mediated ROS activity has been strongly correlated with antibacterial and anticancer efficacy in previous studies.[42–44]

4.2. Fourier transform infrared (FTIR) spectroscopy study

The FTIR spectra offer valuable insights into the functional groups and interactions within the composite material.[45] Fig. 2 displays FTIR spectra of ESF, ZnO NPs and ESF@ZnO NPs. It can be observed from Fig. 2(a) that ESF displays distinct peaks, with each peak corresponding to unique functional groups. The peak visible at 3280 cm^{-1} suggests the existence of C–H stretching originating from the tyrosine found in the ESF.[46] The three key amide regions for ESF, amide I (1700–1600 cm^{-1}), amide II (1600–1500 cm^{-1}) and amide III (1350–1250 cm^{-1}) lie in the band region from 2000–1000 cm^{-1}.[47] The majority of the amide I area is mostly caused by the C=O stretching vibration, with the remaining portion resulting from NH in-plane bending, out-of-phase CN stretching vibration, and C–CN deformation.[40] The backbone oscillations in the CN stretching and NH in-plane bending regions comprise the amide II region.[47] Amide III peaks arise from the concurrent presence of in-phase N–H in-plane bending vibrations, C–N stretching, and C–H/N–H deformation vibrations.[48] It can be observed from Fig. 2(b) that three distinct peaks are observed in the ZnO NPs spectrum. The signal observed at 3384 and 2890 cm^{-1} is associated with stretching vibrations of O–H bonds which indicate the existence of hydroxyl groups or water molecules.[49] The peaks observed at 1643 and 1441 cm^{-1} are attributed to the stretching vibrations of C=C bonds.[50] The peaks at 885 and 696 cm^{-1} indicate the stretching vibrations of Zn–O bonds, thereby proving the presence of ZnO NPs in the sample.[51]

It can be observed from Fig. 2(c) that ESF@ZnO NPs exhibit characteristics from both ESF and ZnO NPs, suggesting that the two materials have been effectively combined. The bio-nanocomposite exhibits peaks at amide I, II and III regions, which indicates the presence of ESF in the sample. However, the peaks observed have low intensity in comparison to the pure ESF, suggesting that the change in the ESF matrix is due to the chemical interaction with ZnO NPs. The composite spectra clearly show peaks at 885 and 696 cm^{-1}, which are indicative of ZnO NPs. This confirms that ZnO NPs have been incorporated into the ESF matrix. Moreover, the ESF@ZnO NPs spectra display novel peaks and broadening of peaks, suggesting possible chemical interactions or structural modifications resulting from the amalgamation of ESF and ZnO NPs. Such changes can enhance the surface reactivity and exposure of functional groups, which are crucial for biological interactions. The observed broad O–H and Zn–O bonding suggests increased availability of sites for hydrogen bonding and electrostatic interactions with bacterial and cancer cell membranes for activity.[52]

4.3. Ultraviolet-visible (UV-vis) spectroscopy study

UV-vis spectroscopy was performed to confirm the presence of ZnO NPs in the ESF matrix. Fig. 3 shows the UV-vis graphs of ESF, ZnO NPs and ESF@ZnO NPs. As can be observed from Fig. 3(a) ESF shows absorption peaks at 219 nm, which are commonly linked to n–π* transitions in the main chain of the peptide bond.[53] These peaks indicate the existence of conjugated systems or chromophoric groups within the ESF structure. This peak is attributed to the presence of the peptide bond in the main chain.[54] Also, it can be observed from Fig. 3(b) that ZnO NPs show a peak at around 343 nm which confirms the formation of ZnO NPs.[55] The blue shift near band edge UV-vis absorption of ZnO NPs was due to the quantum confinement effect of ZnO NPs.[55] As can be seen from Fig. 3(c) the absorption spectra of the composite ESF@ZnO NPs display a wide absorbance peak, indicating the successful integration of ZnO NPs into the ESF matrix. In addition, any changes in the absorbance peaks or broadening detected in the composite spectrum may suggest interactions between ESF and ZnO NPs, such as alterations in the electronic surroundings or the creation of new hybrid states. It can be seen from Fig. 3(c) that ESF@ZnO NPs show the presence of both ESF and ZnO NPs which indicates the successful integration of ZnO NPs into the ESF matrix. Also, the shift in the position of the peak and change in the intensity of ZnO NPs suggest successful interaction between ZnO NPs and ESF.

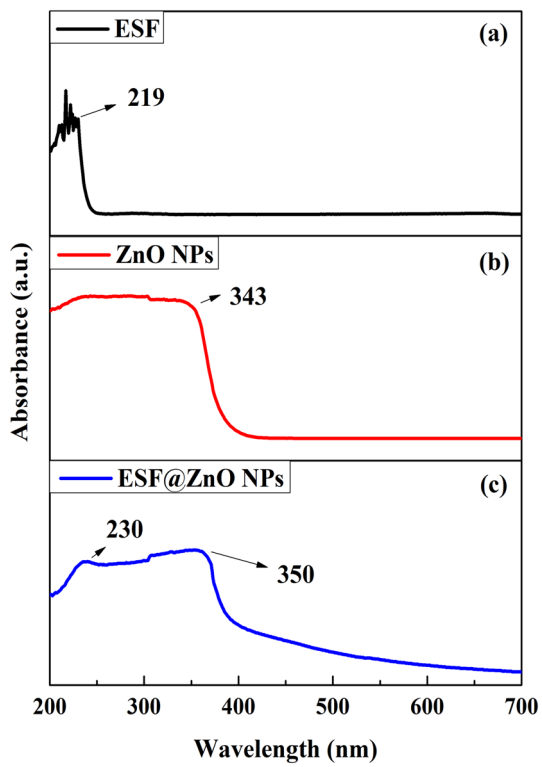

Fig. 3 UV-vis of (a) ESF, (b) ZnO NPs and (c) ESF@ZnO NPs.

4.4. Field emission scanning electron microscopy (FESEM)-energy dispersive spectroscopy (EDS) study

FESEM and EDS were performed to study the surface morphology and elemental composition of ESF, ZnO NPs and ESF@ZnO NPs. It can be observed from Fig. 4(a) that pure ESF demonstrates a characteristic interconnected network of fibroin microparticles (0.5–2 μm diameter). EDS (Fig. 5(a)) confirms the proteinaceous composition of ESF with carbon (47.3 wt%), nitrogen (23.9 wt%) and oxygen (28.9 wt%). In contrast, ZnO NPs appeared as aggregated nanoparticles with radially arranged nanoflakes having a size of 100–200 nm (Fig. 4(b)). These nanoflakes exhibit sharp edges and thin plate-like structures which indicates anisotropic crystal growth. Flake-like morphologies often provide higher surface-to-volume ratios and more exposed reactive edge/facet sites compared with simple spherical or rod shapes, which can enhance ion release and ROS generation, mechanisms linked to antibacterial and anticancer action.[56,57] Comparative studies have reported enhanced bioactivity for flake-like ZnO *versus* spherical/rod forms; our morphological observations therefore provide a plausible structural basis for the improved activity of ESF@ZnO. EDS reveals stoichiometric zinc (71 wt%) and oxygen (29 wt%) contents (Fig. 5(b)). Fig. 4(c) illustrates the FESEM image of ESF@ZnO NPs. It shows an irregular porous surface morphology where ZnO NPs are distributed throughout the protein matrix of ESF. Compared to pure ZnO nanoflake structure, the flakes appear more embedded and less defined which suggests encapsulation or surface coverage by the fibroin phase. The surface texture is relatively rough, and the presence of aggregated clusters indicates possible crosslinking or entanglement between the ZnO flakes and the protein chains, resulting in a heterogeneous structure. The EDS result of ESF@ZnO NPs also confirms the hybrid composition (carbon: 45.1 wt%, nitrogen: 3.4 wt%, oxygen: 31.2 wt%, zinc: 20.2 wt%) (Fig. 5(c)). The preserved nitrogen content confirms the structural integrity of ESF. Oxygen enrichment against the pure ESF and ZnO reflected contributions from both ESF and ZnO phases. Table 1 highlights the weight percentage of different components in ESF, ZnO and ESF@ZnO. Therefore, FESEM confirms the dual phase nature of ESF@ZnO, where ZnO NPs anchor within the ESF matrix without altering the protein's primary content.

4.5. Transmission electron microscopy (TEM) study

The formation and crystallinity of ZnO and ESF@ZnO NPs were further confirmed by the TEM images and SAED patterns. It can be observed from Fig. 6(a and b) that TEM further supports the flake like morphology of ZnO NPs at the nanoscale. It is clear from the figure that flakes possess irregular boundaries. The corresponding SAED (Selected Area Electron Diffraction) pattern (Fig. 6(c)) exhibits a set of concentric rings with bright and well-defined diffraction spots which is a characteristic of polycrystalline ZnO structures.[58] It confirms that the synthesized ZnO flakes are composed of nanocrystalline domains oriented in multiple directions but maintaining a wurtzite crystal structure. The TEM images (Fig. 6(d and e) of ESF@ZnO also confirm the hybrid nature of the nanocomposite. Electron dense ZnO flakes

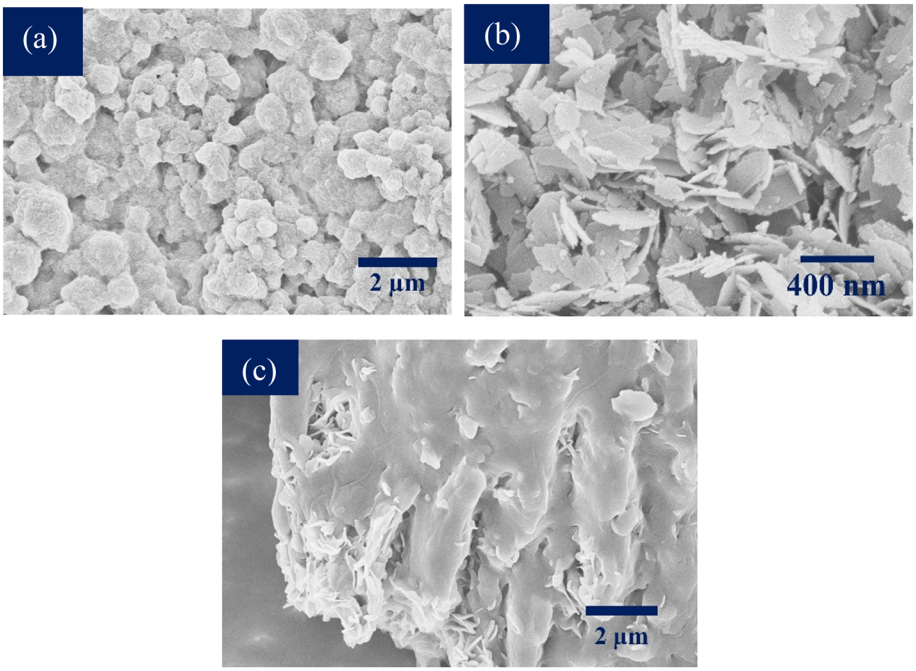

Fig. 4 FESEM images of (a) ESF, (b) ZnO NPs and (c) ESF@ZnO NPs.

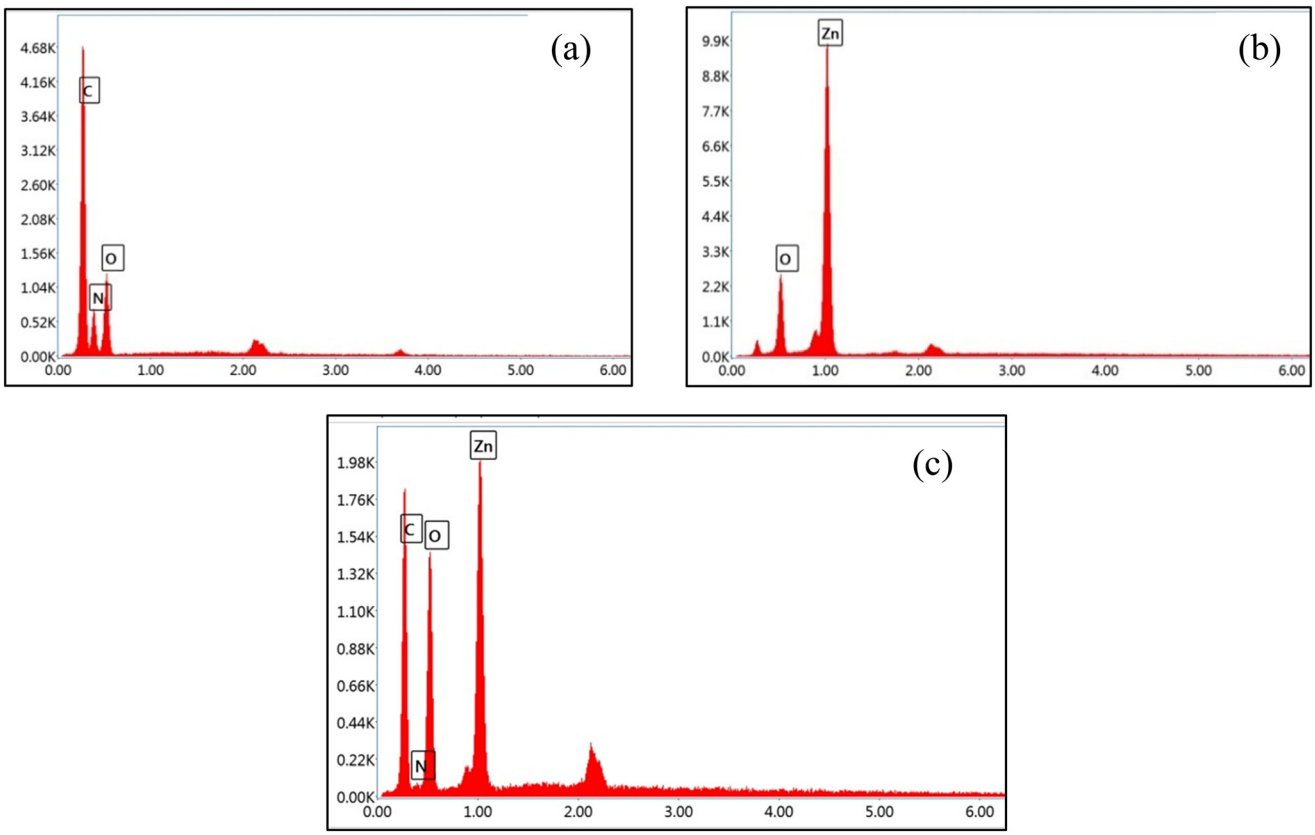

Fig. 5 EDS of (a) ESF, (b) ZnO NPs and (c) ESF@ZnO NPs.

are well dispersed within the lighter amorphous protein matrix of ESF. The SAED pattern (Fig. 6(f)) also exhibits both crystalline and amorphous features. The diffused halos correspond to the disordered and non-crystalline nature of ESF, whereas

Table 1 Elemental composition (wt%)

Element	ESF	ZnO NPs	ESF@ZnO NPs
Carbon	47.3	—	45.1
Nitrogen	23.9	—	3.4
Oxygen	28.9	29	31.2
Zinc	—	71	20.2

superimposed bright rings illustrate wurtzite ZnO NPs, particularly the (100) and (101) planes, as shown in the figure. This confirms that ZnO retains its crystalline phase post integration while ESF maintains its amorphous nature. The improved dispersion of ZnO nanoparticles within the ESF matrix may enhance the effective surface area for interaction with bacterial cell walls and cancer cell membranes providing good antibacterial and anticancer activities.[59] In addition, the effective dispersion of ZnO within the silk fibroin matrix, as evidenced by FESEM (Fig. 4), EDS (Fig. 5) and TEM (Fig. 6) analyses, indicates a stable hybrid structure with strong electrostatic interactions between the protein's functional groups and ZnO nanoparticles.

5. Applications

5.1. Antibacterial activity

The antimicrobial activity of the bio-nanocomposite material ESF@ZnO NPs was methodically assessed against two bacterial strains: *Escherichia coli* (*E. coli*) and *Bacillus subtilis* (*B. subtilis*), utilizing the standard inhibition zone method. Standard antibiotics were used as positive control for both strains. For *E. coli* penicillin was used and for *B. subtilis* gentamicin was used. Fig. 7(a and b) shows the inhibition zone against *E. coli* and *B. subtilis*. The antibacterial study revealed that pure ESF exhibited no inhibitory effect against *E. coli* and *B. subtilis*, which aligns with its known biocompatibility and lack of inherent antimicrobial properties. In contrast, pure ZnO NPs demonstrated moderate antibacterial activity, with inhibition zones of 11.2 ± 0.20 mm for *E. coli* and 11.6 ± 0.11 mm for *B. subtilis*, indicating their intrinsic ability to suppress bacterial growth. The enhanced antibacterial performance of ESF@ZnO NPs, with inhibition zones of 14.8 ± 0.15 mm (*E. coli*) and 13.2 ± 0.14 mm (*B. subtilis*), suggests a synergistic interaction between ESF and ZnO that significantly boosts antimicrobial efficacy. For comparison, penicillin (positive control for *E. coli*) exhibited a smaller inhibition zone of 7.8 ± 0.43 mm, while ampicillin (positive control for *B. subtilis*) showed a larger zone of 15.1 ± 0.65 mm. The results of the inhibitory zone have been compiled and are displayed in Fig. 8.

The difference in inhibition zones between *E. coli* (Gram-negative) and *B. subtilis* (Gram-positive) can be attributed to structural variations in their cell walls. Gram-negative bacteria possess a thin peptidoglycan cell wall layer (<10 nm) and an extra outer membrane composed of lipopolysaccharides (LPS) (~7 nm), featuring many holes and appendages.[60] Conversely, Gram-positive bacteria possess a thick cell wall (20–80 nm) as the outermost layer of the cell.[60] The variations in cell layer characteristics correspond to distinct aspects of the cell,

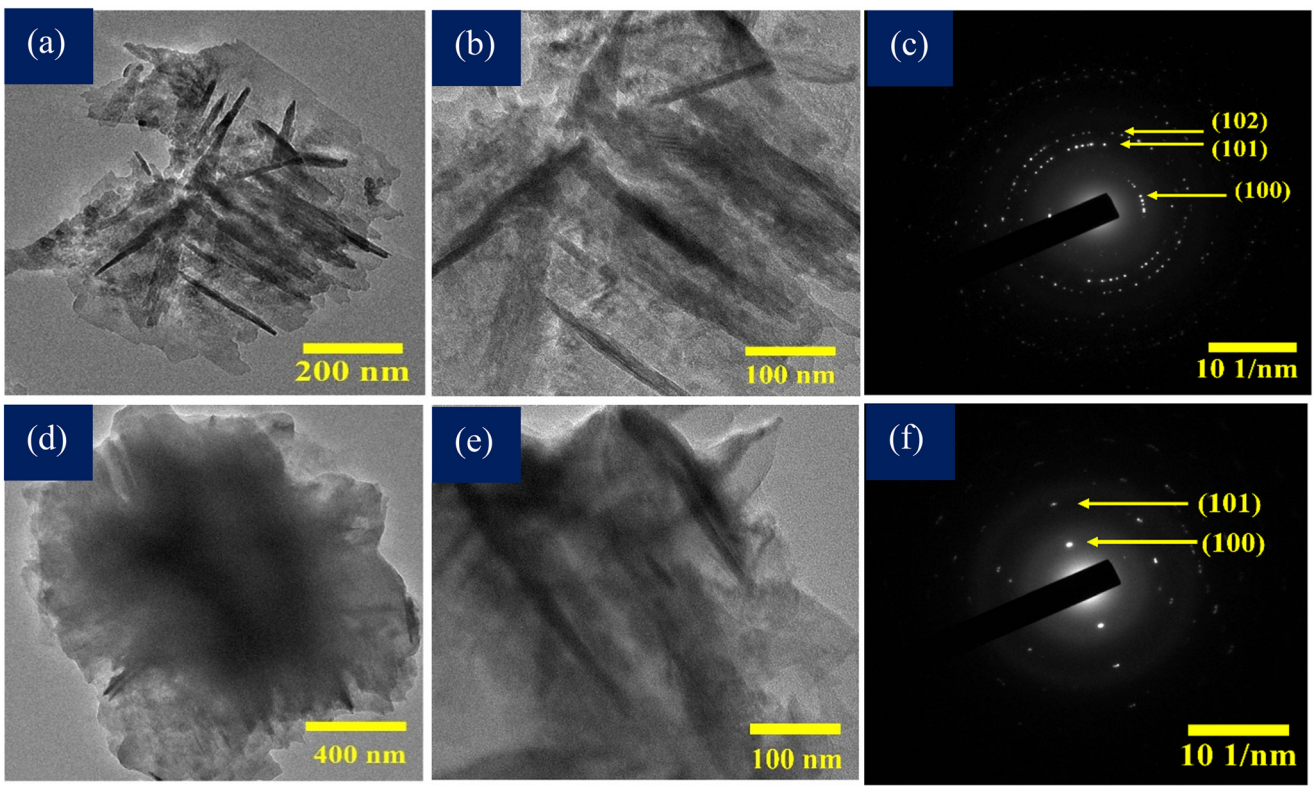

Fig. 6 (a and b) TEM images of ZnO NPs. (c) SAED pattern of ZnO NPs. (d and e) TEM images of ESF@ZnO NPs. (f) SAED pattern of ESF@ZnO NPs.

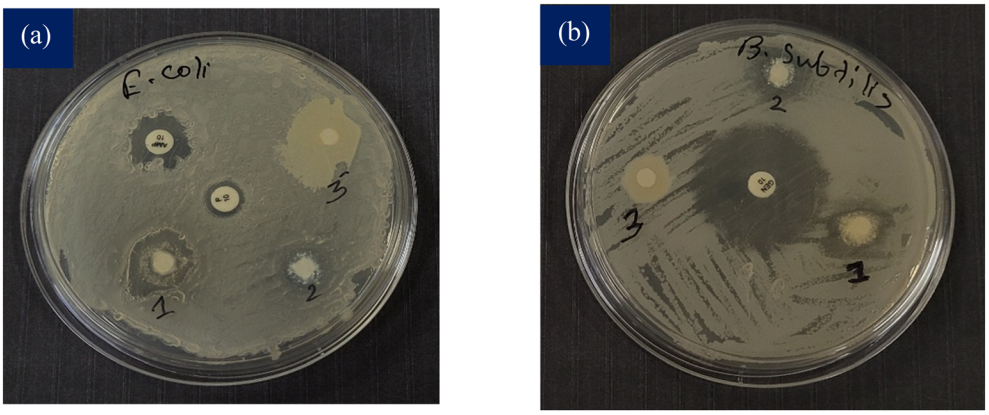

Fig. 7 Antibacterial activity against (a) *E. coli* and (b) *B. subtilis*. The spots (1, 2 and 3) indicated ESF@ZnO NPs, ZnO NPs and ESF, respectively. The remaining zone illustrates the positive control (ampicillin and penicillin).

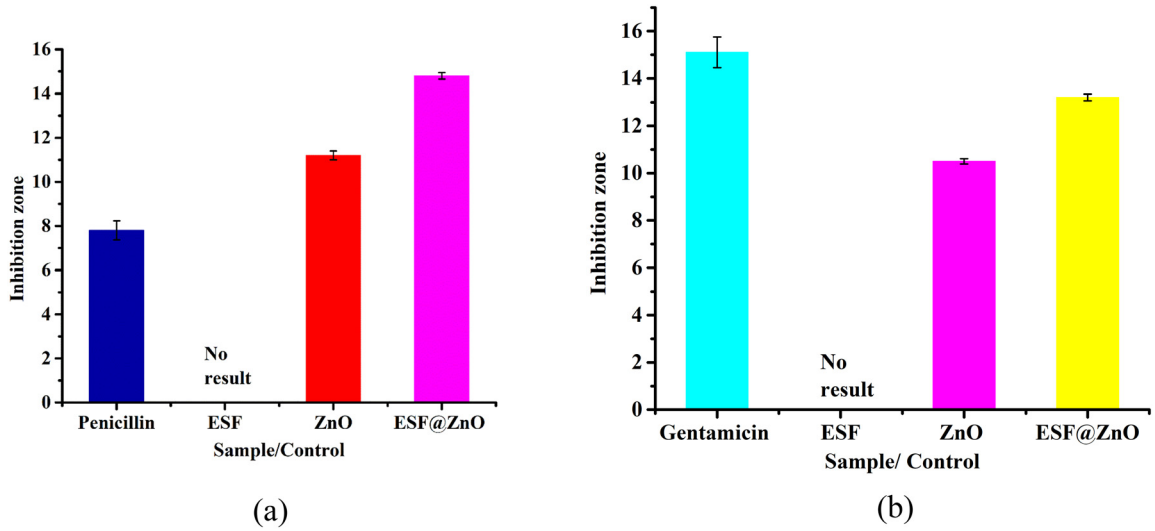

Fig. 8 Zones of inhibition of ESF, ZnO and ESF@ZnO against (a) *E. coli* and (b) *B. subtilis*. Penicillin and gentamicin were used as positive controls for *E. coli* and *B. subtilis*, respectively.

especially in response to external disruptions or stresses, such as antibiotics. Multiple mechanisms are involved in the antibacterial effect of ZnO NPs. The initial physical interaction between ZnO NPs and bacterial cells leads to direct engagement of ZnO NPs with the bacterial membrane, resulting in membrane destruction and cell death.[61] Various reasons have been postulated for the attachment of ZnO NPs to bacterial cell surfaces, such as van der Waals forces, electrostatic interactions, hydrophobic contacts, and receptor–ligand interactions.[62] ZnO NPs also produce reactive oxygen species (ROS) such as hydroxyl radicals (OH^-) which interact with the bacterial cells and damage them.[61] When ZnO NPs are combined with ESF to form ESF@ZnO NPs, several key enhancements occur. The ESF matrix improves nanoparticle dispersion and prevents ZnO NP agglomeration for bacterial interaction.[63] Additionally, the proteinaceous composition of ESF adheres it to the bacterial cell surface and binds it to membranes more strongly, concentrating the effects of ZnO NPs and enhancing ROS at the cell surface. Thus, ESF@ZnO NPs amplifies these effects through improved stability, controlled ion release, and enhanced bacterial adhesion, making it a more potent antibacterial agent and underscores its broad-spectrum potential.

5.2. Anticancer activity

The cytotoxic effects of pure ESF and ESF@ZnO NPs were assessed in two distinct breast cancer cell lines: 4T1 (BALB/c strain mouse breast cancer cell line) and MDA-MB-231 (human triple-negative breast cancer cell line). The viability of cells was evaluated after treatment with different concentrations of pure ESF and ESF@ZnO NPs, and the half-maximal inhibitory concentration (IC_{50}) values were calculated to assess their relative effectiveness. Fig. 9 shows the cell viability against 4T1 cells for both ESF and ESF@ZnO NPs. It can be observed from Fig. 9(a) that in 4T1 cells, ESF showed no significant cytotoxic

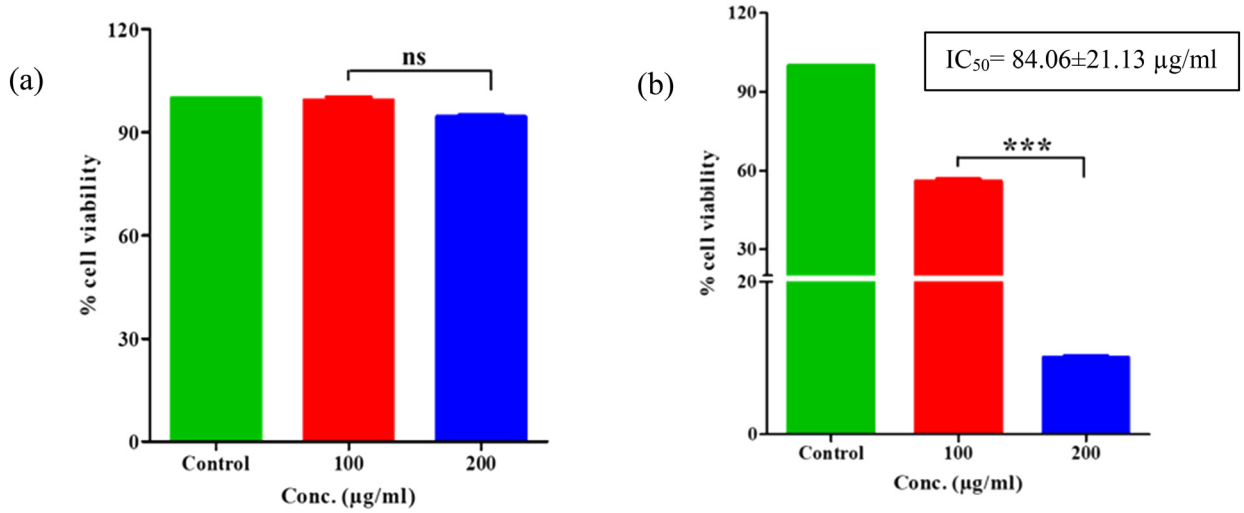

Fig. 9 The effect of (a) ESF and (b) ESF@ZnO NPs on cell viability of 4T1 cells after 24 hours of treatment. The graphs were plotted as mean ± SEM, $n = 3$. ***$p < 0.001$.

effects, with cell viability remaining similar to the control even at the highest concentrations tested. Conversely, Fig. 9(b) reveals that ESF@ZnO demonstrates an IC_{50} of 84.06 ± 21.13 µg mL^{-1} against the 4T1 cells, suggesting cytotoxicity effects. A distinct dose-dependent cytotoxicity trend was noted, showing a substantial decrease in cell viability at concentrations of 100 and 200 µg ml^{-1} ($p < 0.001$). At a concentration of 200 µg mL^{-1}, cell viability was almost completely eliminated, indicating that at high concentrations, ESF@ZnO NPs can significantly impede the growth of 4T1 cells. In MDA-MB-231 cells (Fig. 10(a)), surprisingly pure ESF demonstrated an IC_{50} of 68.93 µg mL^{-1}, suggesting that elevated concentrations were necessary to elicit notable cytotoxic effects. At a concentration of 100 µg ml^{-1}, cell viability was still notably high, indicating that pure ESF exhibits limited anticancer activity. On the other hand, Fig. 10(b) shows that ESF@ZnO NPs exhibits a significantly lower IC_{50} of 29.76 ± 13.46 µg mL^{-1}, suggesting increased cytotoxicity as a result of ZnO incorporation. A clear reduction in cell viability was noted in a dose-dependent manner, with statistically significant differences ($p < 0.001$) evident at elevated concentrations. The results indicate that ESF@ZnO NPs markedly shows good anticancer efficacy in comparison to pure ESF, positioning it as a promising option for breast cancer treatment.

ESF@ZnO NPs exhibits anticancer activity through a multi-faceted mechanism involving enhanced cellular uptake, ROS-mediated oxidative stress, mitochondrial dysfunction, DNA damage, and apoptosis induction.[43] ESF acts as a biocompatible matrix that facilitates the dispersion and stabilization of ZnO NPs, allowing for efficient cellular uptake.[64] Additionally, Eri silk fibroin (ESF) is a natural protein with proven cytocompatibility

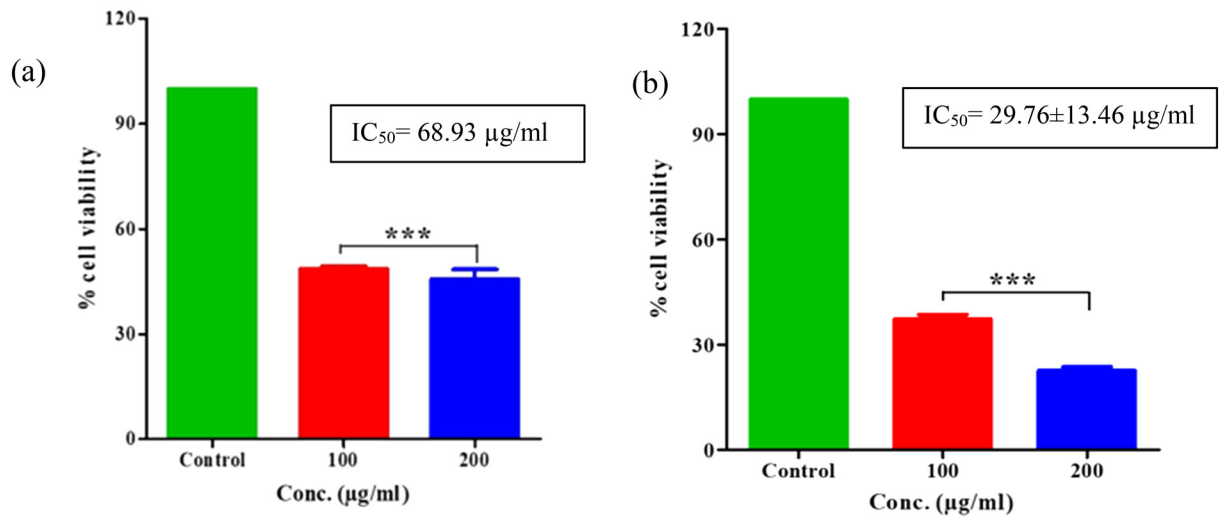

Fig. 10 The effect of (a) ESF and (b) ESF@ZnO NPs on cell viability of MDA-MB-231 cells after 24 hours of treatment. The graphs were plotted as mean ± SEM, $n = 3$. ***$p < 0.001$.

and ZnO nanoparticles have been reported to exhibit selective cytotoxicity toward malignant cells due to their greater sensitivity to oxidative stress.[18,19,21,65,66] Cancer cells, due to their altered membrane structure and metabolic activity, show higher endocytosis rates compared to normal cells.[67] When ZnO NPs enter the cellular environment, they interact with the lipid bilayer and penetrate the cytoplasm through endocytosis.[68] ZnO NPs are known to generate ROS, including peroxide (O_2^{2-}), hydroxyl radicals (OH^-), and hydrogen peroxide (H_2O_2), upon exposure to the cellular environment.[44] These ROS cause oxidative stress, damaging essential cellular components such as proteins, lipids, and nucleic acids.[69] ROS-mediated oxidative damage induces strand breaks in DNA, triggering checkpoint mechanisms that halt cell cycle progression.[69] This prevents cancer cell proliferation and promotes apoptosis.[70] The interaction of ZnO NPs with DNA can further disrupt transcription and replication, contributing to cytotoxic effects.[71] Thus, ESF provides a platform that enhances the stability and bioavailability of ZnO NPs. Unlike direct ZnO NP exposure, which may cause excessive toxicity, the ESF matrix ensures a controlled and sustained release of ZnO NPs, reducing undesirable side effects. Additionally, ESF contains amino acid sequences that may facilitate cellular adhesion and uptake, improving the composite's interaction with cancer cells while maintaining minimal toxicity to normal cells.[66]

6. Conclusion

This study successfully developed and characterized ESF@ZnO NPs, demonstrating its potential for antibacterial and anticancer applications. The PXRD analysis confirmed the crystalline and amorphous portions of ESF@ZnO NPs. UV-vis spectroscopy showed the simultaneous presence of ZnO NPs and ESF in the bio-nanocomposite. FTIR analysis further validated the successful formation of the bio-nanocomposite, highlighting key functional group interactions. FESEM and TEM analyses confirmed the successful integration of ZnO nanoflakes into the ESF matrix. FESEM showed a rough, heterogeneous surface, while TEM revealed well-dispersed crystalline ZnO NPs within the amorphous fibroin phase of ESF. This hybrid structure enhances surface interaction, supporting the composite's antibacterial activity through controlled and sustained ROS generation and its anticancer effect *via* improved cellular uptake and cytotoxicity. ESF@ZnO NPs exhibited enhanced antibacterial activity against *E. coli* in comparison to *B. subtilis* and as a whole strong potential for antibacterial applications. ESF@ZnO NPs demonstrates anticancer efficacy against 4T1 (BALB/c strain mouse breast cancer) and MDA-MB-231 (human triple-negative breast cancer) cell lines. A dose-dependent reduction in cell viability was observed, with statistically significant cytotoxic effects ($p < 0.001$) at higher concentrations, confirming the effectiveness of ESF@ZnO NPs in inducing cancer cell death. The IC_{50} value of ESF@ZnO NPs was determined to be 84.06 ± 21.13 μg mL^{-1} for 4T1 cells and 29.76 ± 13.46 μg mL^{-1} for MDA-MB-231 cells, highlighting its potent anticancer activity, particularly against MDA-MB-231 cells. These findings suggest that ESF@ZnO NPs holds strong potential for future biomedical applications.

Conflicts of interest

There are no conflicts of declare.

Data availability

Data for this article, including XRD, FTIR, UV-Vis, FESEM and TEM are available at Zenodo repository at https://doi.org/10.5281/zenodo.17781101.

Acknowledgements

The authors extend their thanks to the Central Instrumentation Facility (CIF) at Gauhati University, SAIC at IASST, and the Department of Chemistry, CITK, for their assistance in sample analysis. The authors also acknowledge Northeast Centre for Biological Sciences and Healthcare Engineering (NECBH), IIT Guwahati and Department of Biotechnology (DBT), Govt. of India for project no. BT/NER/143/SP44675/2023 for the FESEM instrumentation facility.

References

1 S. J. Dunachie, N. P. Day and C. Dolecek, The challenges of estimating the human global burden of disease of antimicrobial resistant bacteria, *Curr. Opin. Microbiol.*, 2020, **57**, 95–101, DOI: 10.1016/j.mib.2020.09.013.
2 A. Marra, D. Trapani, G. Viale, C. Criscitiello and G. Curigliano, Practical classification of triple-negative breast cancer: intratumoral heterogeneity, mechanisms of drug resistance, and novel therapies, *npj Breast Cancer*, 2020, **6**(1), 1–16, DOI: 10.1038/s41523-020-00197-2.
3 J. Tanwar, S. Das, Z. Fatima and S. Hameed, Multidrug resistance, An emerging crisis, *Interdiscip. Perspect. Infect. Dis.*, 2014, **2014**, 541340.
4 Organization WH, *Antimicrobial resistance*, 2023, Available from: https://www.who.int/news-room/fact-sheets/detail/antimicrobial-resistance.
5 S. Chanel and B. Doherty, The guardian, 2020, "Superbugs" a far greater risk than Covid in Pacific, scientist warns, Available from: https://www.theguardian.com/world/2020/sep/10/superbugs-a-far-greater-risk-than-covid-in-pacific-scientist-warns.
6 V. Ozkocaman, T. Ozcelik, R. Ali, F. Ozkalemkas, A. Ozkan and C. Ozakin, *et al.*, Bacillus spp. among hospitalized patients with haematological malignancies: clinical features, epidemics and outcomes, *J. Hosp. Infect.*, 2006, **64**(2), 169–176.
7 WHO, Cancer, 2025, Available from: https://www.who.int/news-room/fact-sheets/detail/cancer.
8 E. Orrantia-Borunda, P. Anchondo-Nunez, L. E. Acuna-Aguilar, F. O. Gomez-Valles and C. A. Ramirez-Valdespino, Subtypes of Breast Cancer, in *Breast Cancer*, ed. H. N. Mayrovitz, Brisbane, Australia, 2022, Available from: https://www.ncbi.nlm.nih.gov/books/NBK583808/.

9 L. Yin, J. J. Duan, X. W. Bian and S. C. Yu, Triple-negative breast cancer molecular subtyping and treatment progress, *Breast Cancer Res.*, 2020, **22**(1), 1–13.
10 J. J. Arroyo-Crespo, A. Armiñán, D. Charbonnier, C. Deladriere, M. Palomino-Schätzlein and R. Lamas-Domingo, *et al.*, Characterization of triple-negative breast cancer preclinical models provides functional evidence of metastatic progression, *Int. J. Cancer*, 2019, **145**(8), 2267–2281.
11 M. Wypij, T. Jędrzejewski, J. Trzcińska-Wencel, M. Ostrowski, M. Rai and P. Golińska, Green Synthesized Silver Nanoparticles: Antibacterial and Anticancer Activities, Biocompatibility, and Analyses of Surface-Attached Proteins, *Front. Microbiol.*, 2021, **12**, 632505.
12 H. Cheng, M. Zhang, H. Hu, Z. Gong, Y. Zeng and J. Chen, *et al.*, Selenium-Modified TiO2 Nanoarrays with Antibacterial and Anticancer Properties for Postoperation Therapy Applications, *ACS Appl. Bio Mater.*, 2018, **1**(5), 1656–1666.
13 R. Rajamma, S. G. Nair, F. A. Khadar and B. Baskaran, Antibacterial and anticancer activity of biosynthesised CuO nanoparticles, *IET Nanobiotechnol.*, 2020, **14**(9), 833–838.
14 S. C. E. González, E. Bolaina-Lorenzo, J. J. Pérez-Trujillo, B. A. Puente-Urbina, O. Rodríguez-Fernández and A. Fonseca-García, *et al.*, Antibacterial and anticancer activity of ZnO with different morphologies: a comparative study, *3 Biotech.*, 2021, **11**(2), 1–12, DOI: 10.1007/s13205-020-02611-9.
15 M. Azizi-Lalabadi, A. Ehsani, B. Divband and M. Alizadeh-Sani, Antimicrobial activity of Titanium dioxide and Zinc oxide nanoparticles supported in 4A zeolite and evaluation the morphological characteristic, *Sci. Rep.*, 2019, **9**(1), 1–10.
16 A. Azam, A. S. Ahmed, M. Oves, M. S. Khan, S. S. Habib and A. Memic, Antimicrobial activity of metal oxide nanoparticles against Gram-positive and Gram-negative bacteria: A comparative study, *Int. J. Nanomed.*, 2012, **7**, 6003–6009.
17 C. R. Mendes, G. Dilarri, C. F. Forsan, M. R. Sapata V de, P. R. M. Lopes and P. B. de Moraes, *et al.*, Antibacterial action and target mechanisms of zinc oxide nanoparticles against bacterial pathogens, *Sci. Rep.*, 2022, **12**(1), 1–10, DOI: 10.1038/s41598-022-06657-y.
18 P. Gopala Krishna, P. Paduvarahalli Ananthaswamy, T. Yadavalli, N. Bhangi Mutta, A. Sannaiah and Y. Shivanna, ZnO nanopellets have selective anticancer activity, *Mater. Sci. Eng., C*, 2016, **62**, 919–926, DOI: 10.1016/j.msec.2016.02.039.
19 H. Moratin, A. Scherzad, T. Gehrke, P. Ickrath, K. Radeloff and N. Kleinsasser, *et al.*, Toxicological characterization of ZnO nanoparticles in malignant and non-malignant cells, *Environ. Mol. Mutagen.*, 2018, **59**(3), 247–259.
20 D. Cao, S. Gong, X. Shu, D. Zhu and S. Liang, Preparation of ZnO Nanoparticles with High Dispersibility Based on Oriented Attachment (OA) Process, *Nanoscale Res. Lett.*, 2019, **14**, 210.
21 Y. Zou, Z. Huang, Y. Wang, X. Liao, G. Yin and J. Gu, Synthesis and cellular compatibility of Co-doped ZnO particles in silk-fibroin peptides, *Colloids Surf., B*, 2013, **102**, 29–36, DOI: 10.1016/j.colsurfb.2012.08.002.
22 N. Ahmad, S. Sultana, S. M. Faisal, A. Ahmed, S. Sabir and M. Z. Khan, Zinc oxide-decorated polypyrrole/chitosan bionanocomposites with enhanced photocatalytic, antibacterial and anticancer performance, *RSC Adv.*, 2019, **9**(70), 41135–41150.
23 P. P. Patil, J. V. Meshram, R. A. Bohara, S. G. Nanaware and S. H. Pawar, ZnO nanoparticle-embedded silk fibroin-polyvinyl alcohol composite film: A potential dressing material for infected wounds, *New J. Chem.*, 2018, **42**(17), 14620–14629.
24 C. M. Yang, J. Lee, S. Y. Lee, H. Lee, K. Chathuranga and J. Lee, *et al.*, Silk Fibroin/Tannin/ZnO Nanocomposite Hydrogel with Hemostatic Activities, *Gels.*, 2022, **8**(10), 650.
25 X. Lian, Y. Li, D. An, Y. Zou, Q. Wang and N. Zhang, Synthesis of porous ZnO nanostructures using bamboo fibers as templates, *Mater. Sci.-Pol.*, 2014, **32**(3), 514–520.
26 P. M. Gore, M. Naebe, X. Wang and B. Kandasubramanian, Progress in silk materials for integrated water treatments: Fabrication, modification and applications, *Chem. Eng. J.*, 2019, **374**, 437–470, DOI: 10.1016/j.cej.2019.05.163.
27 K. Zheng, J. Zhong, Z. Qi, S. Ling and D. L. Kaplan, Isolation of Silk Mesostructures for Electronic and Environmental Applications, *Adv. Funct. Mater.*, 2018, **28**(51), 1–10.
28 Y. Qi, H. Wang, K. Wei, Y. Yang, R. Y. Zheng and I. S. Kim, *et al.*, A review of structure construction of silk fibroin biomaterials from single structures to multi-level structures, *Int. J. Mol. Sci.*, 2017, **18**(3), 237.
29 R. Ranjana, N. Parushuram, K. S. Harisha, S. Asha and Y. Sangappa, Silk fibroin a bio-template for synthesis of different shaped gold nanoparticles: Characterization and ammonia detection application, *Mater. Today: Proc.*, 2020, **27**, 434–439, DOI: 10.1016/j.matpr.2019.11.259.
30 Z. Xu, L. Shi, M. Yang and L. Zhu, Preparation and biomedical applications of silk fibroin-nanoparticles composites with enhanced properties - A review, *Mater. Sci. Eng., C*, 2019, **95**, 302–311, DOI: 10.1016/j.msec.2018.11.010.
31 Y. Z. Zhao, M. T. Lin, Q. H. Lan, Y. Y. Zhai, H. L. Xu and J. Xiao, *et al.*, Silk fibroin-modified disulfiram/zinc oxide nanocomposites for pH triggered release of Zn2+ and synergistic antitumor efficacy, *Mol. Pharmaceutics*, 2020, **17**(10), 3857–3869.
32 T. P. Nguyen, Q. V. Nguyen, V.-H. Nguyen, T.-H. Le, V. Q. N. Huynh, D.-V. N. Vo, Q. T. Trinh, S. Y. Kim and Q. V. Le, Silk Fibroin-Based Biomaterials for Biomedical Applications: A Review, *Polymers*, 2019, **11**, 1933.
33 Y. Xue, F. Wang, M. Torculas, S. Lofland and X. Hu, Formic Acid Regenerated Mori, Tussah, Eri, Thai, and Muga Silk Materials: Mechanism of Self-Assembly, *ACS Biomater. Sci. Eng.*, 2019, **5**(12), 6361–6373.
34 M. Bashi, H. Madanchi and B. Yousefi, Investigation of cytotoxic effect and action mechanism of a synthetic peptide derivative of rabbit cathelicidin against MDA-MB-231 breast cancer cell line, *Sci. Rep.*, 2024, **14**(1), 1–12, DOI: 10.1038/s41598-024-64400-1.
35 Z. G. Gao, L. Tian, J. Hu, I. S. Park and Y. H. Bae, Prevention of metastasis in a 4T1 murine breast cancer model by doxorubicin carried by folate conjugated pH sensitive polymeric micelles, *J. Controlled Release*, 2011, **152**(1), 84–89, DOI: 10.1016/j.jconrel.2011.01.021.

36 S. Shrivastava, P. Kulkarni, D. Thummuri, M. K. Jeengar, V. G. M. Naidu and M. Alvala, *et al.*, Piperlongumine, an alkaloid causes inhibition of PI3 K/Akt/mTOR signaling axis to induce caspase-dependent apoptosis in human triple-negative breast cancer cells, *Apoptosis*, 2014, **19**(7), 1148–1164.
37 G. Fotakis and J. A. Timbrell, In vitro cytotoxicity assays: Comparison of LDH, neutral red, MTT and protein assay in hepatoma cell lines following exposure to cadmium chloride, *Toxicol. Lett.*, 2006, **160**(2), 171–177.
38 M. Andiappan, S. Sundaramoorthy, N. Panda, G. Meiyazhaban, S. B. Winfred and G. Venkataraman, *et al.*, Electrospun eri silk fibroin scaffold coated with hydroxyapatite for bone tissue engineering applications, *Prog. Biomater.*, 2013, **2**(1), 1–11.
39 H. A. Varudkar, G. Umadevi, P. Nagaraju, J. S. Dargad and V. D. Mote, Fabrication of Al-doped ZnO nanoparticles and their application, *J. Mater. Sci.: Mater. Electron.*, 2024, **9**(4), 623–658.
40 B. Bhushan, P. Kalita and B. M. Baruah, Physical Analysis of White and Brick Red Eri Silk Fiber, *Fibers Polym.*, 2025, 0123456789, DOI: 10.1007/s12221-025-00958-5.
41 Y. Li, Z. Ren, Z. He, P. Ouyang, Y. Duan and W. Zhang, *et al.*, Crystallinity-defect matching relationship of g-C3N4: Experimental and theoretical perspectives, *Green Energy Environ.*, 2024, **9**(4), 623–658, Available from: https://www.sciencedirect.com/science/article/pii/S2468025723000365.
42 V. Lakshmi Prasanna and R. Vijayaraghavan, Insight into the Mechanism of Antibacterial Activity of ZnO: Surface Defects Mediated Reactive Oxygen Species Even in the Dark, *Langmuir*, 2015, **31**(33), 9155–9162, DOI: 10.1021/acs.langmuir.5b02266.
43 V. Sharma, D. Anderson and A. Dhawan, Zinc oxide nanoparticles induce oxidative DNA damage and ROS-triggered mitochondria mediated apoptosis in human liver cells (HepG2), *Apoptosis*, 2012, **17**(8), 852–870.
44 S. Jiang, K. Lin and M. Cai, ZnO Nanomaterials: Current Advancements in Antibacterial Mechanisms and Applications, *Front. Chem.*, 2020, **8**, 1–5.
45 M. K. B. Bakri and E. Jayamani, Comparative Study of Functional Groups in Natural Fibers: Fourier Transform Infrared Analysis (FTIR), *International Journal of Current Engineering and Technology*, 2016, 167–174, Available from: http://www.troindia.in/proceeding/vol-1proceeding.pdf#page=186.
46 P. R. Laity, S. E. Gilks and C. Holland, Rheological behaviour of native silk feedstocks, *Polymer*, 2015, **67**, 28–39, DOI: 10.1016/j.polymer.2015.04.049.
47 A. Barth, The infrared absorption of amino acid side chains, *Prog. Biophys. Mol. Biol.*, 2000, **74**(3–5), 141–173.
48 H. H. Mantsch and L. A. Nafie, Society of Photo-optical Instrumentation Engineers Content Provider, Society of Photo Optical Instrumentation Engineers Content Provider, & Biomedical Optics Society Content Provider, *Proceedings of biomolecular spectroscopy III: 17–18 January 1993*, SPIE Digital Library, Los Angeles, California, 1993, vol. 1890, p. 146.
49 N. Jayarambabu, Ȧ. Nj, Ȧ. B. Siva Kumari, Ḃ. K. Venkateswara Rao and Ḃ. Ȧ. Y. Prabhu, Germination and Growth Characteristics of Mungbean Seeds (Vigna radiata L.) affected by Synthesized Zinc Oxide Nanoparticles, *Int. J. Curr. Eng. Technol.*, 2014, **4**(5), 3411–3416, Available from: http://inpressco.com/category/ijcet.
50 S. Rahemi Ardekani, A. Sabour Rouhaghdam and M. Nazari, N-doped ZnO-CuO nanocomposite prepared by one-step ultrasonic spray pyrolysis and its photocatalytic activity, *Chem. Phys. Lett.*, 2018, **705**, 19–22, DOI: 10.1016/j.cplett.2018.05.052.
51 S. Bashir, M. S. Awan, M. A. Farrukh, R. Naidu, S. A. Khan and N. Rafique, *et al.*, In-vivo (Albino Mice) and in-vitro Assimilation and Toxicity of Zinc Oxide Nanoparticles in Food Materials, *Int. J. Nanomed.*, 2022, **17**, 4073–4085.
52 H. Sheng, K. Nakamura, T. Kanno, K. Sasaki and Y. Niwano, Microbicidal Activity of Artificially Generated Hydroxyl Radicals, in *Interface Oral Health Science 2014*, ed. K. Sasaki, O. Suzuki and N. Takahashi, Springer Japan, Tokyo, 2015, pp. 203–215.
53 J. Ashenhurst, UV-Vis Spectroscopy: Absorbance of Carbonyls - Master Organic Chemistry [Internet], 2024, Available from: https://www.masterorganicchemistry.com/2016/09/26/uv-vis-spectroscopy-absorbance-of-carbonyls/.
54 K. Sen and K. M. Babu, Studies on Indian Silk. I. Macrocharacterization and Analysis of Amino Acid Composition, *J. Appl. Polym. Sci.*, 2004, **92**(2), 1080–1097.
55 M. Vaseem, K. M. Lee, J. K. Shin and Y. B. Hahn, Synthesis of ZnO nanoparticles and their ink-jetting behavior, *J. Nanosci. Nanotechnol.*, 2012, **12**(3), 2380–2386.
56 S. C. E. González, E. Bolaina-Lorenzo, J. J. Pérez-Trujillo, B. A. Puente-Urbina, O. Rodríguez-Fernández and A. Fonseca-García, *et al.*, Antibacterial and anticancer activity of ZnO with different morphologies: a comparative study, *3 Biotech.*, 2021, **11**(2), 68, DOI: 10.1007/s13205-020-02611-9.
57 A. Sirelkhatim, S. Mahmud, A. Seeni, N. H. M. Kaus, L. C. Ann and S. K. M. Bakhori, *et al.*, Review on zinc oxide nanoparticles: Antibacterial activity and toxicity mechanism, *Nano-Micro Lett.*, 2015, **7**(3), 219–242, DOI: 10.1007/s40820-015-0040-x.
58 S. Radha, J. Mani, R. Rajavel, M. Arivanandhan, R. Jayavel and G. Anbalagan, Investigation of Structural, Morphological, Thermal, and Thermoelectric Properties of Zn1-xCuxAl2O4 ($0.0 \leq x \leq 0.1$), *Mater. Res. Express*, 2023, **10**(2), 025501.
59 S. Akhtar and F. Zuhair, Advancing Nanomedicine Through Electron Microscopy: Insights Into Nanoparticle Cellular Interactions and Biomedical Applications, *Int. J. Nanomed.*, 2025, **20**, 2847–2878.
60 A. Mai-Prochnow, M. Clauson, J. Hong and A. B. Murphy, Gram positive and Gram negative bacteria differ in their sensitivity to cold plasma, *Sci. Rep.*, 2016, **6**, 1–11.
61 Y. Jiang, L. Zhang, D. Wen and Y. Ding, Role of physical and chemical interactions in the antibacterial behavior of ZnO nanoparticles against E. coli, *Mater. Sci. Eng., C*, 2016, **69**, 1361–1366, DOI: 10.1016/j.msec.2016.08.044.
62 R. Bos, H. C. Van Der Mei and H. J. Busscher, Physico-chemistry of initial microbial adhesive interactions-its

mechanisms and methods for study, *FEMS Microbiol. Rev.*, 1999, **23**, 179–230.

63 C. Dumitriu, A. Constantinescu, A. Dumitru and C. Pîrvu, Modified Electrode with ZnO Nanostructures Obtained from Silk Fibroin for Amoxicillin Detection, *Crystals*, 2022, **12**(11), 1511.

64 J. Kundu, C. Y. Il, Y. H. Kim, G. Tae and S. C. Kundu, Silk fibroin nanoparticles for cellular uptake and control release, *Int. J. Pharm.*, 2010, **388**(1–2), 242–250.

65 J. Kundu, Y. I. Chung, Y. H. Kim, G. Tae and S. C. Kundu, Silk fibroin nanoparticles for cellular uptake and control release, *Int. J. Pharm.*, 2010, **388**(1), 242–250, Available from: https://www.sciencedirect.com/science/article/pii/S0378517310000050.

66 G. De Giorgio, B. Matera, D. Vurro, E. Manfredi, V. Galstyan and G. Tarabella, *et al.*, Silk Fibroin Materials: Biomedical Applications and Perspectives, *Bioengineering*, 2024, **11**(2), 167.

67 A. Choromańska, A. Chwiłkowska, J. Kulbacka, D. Baczyńska, N. Rembiałkowska and A. Szewczyk, *et al.*, Modifications of plasma membrane organization in cancer cells for targeted therapy, *Molecules*, 2021, **26**(7), 1850.

68 S. Dey and D. Mohanty, *et al.*, A critical review on zinc oxide nanoparticles: Synthesis, properties and biomedical applications, *Intell. Pharm.*, 2024, **3**(1), 53–70, DOI: 10.1016/j.ipha.2024.08.004.

69 C. Andrés Juan, J. M. Pérez de la Lastra, F. J. Plou, E. Pérez-Lebeña and S. Reinbothe, Molecular Sciences The Chemistry of Reactive Oxygen Species (ROS) Revisited: Outlining Their Role in Biological Macromolecules (DNA, Lipids and Proteins) and Induced Pathologies, *Int. J. Mol. Sci.*, 2021, **22**, 4642, DOI: 10.3390/ijms.

70 H. Nakamura and K. Takada, Reactive oxygen species in cancer: Current findings and future directions, *Cancer Sci.*, 2021, **112**(10), 3945–3952.

71 P. J. Moos, K. Olszewski, M. Honeggar, P. Cassidy, S. Leachman and D. Woessner, *et al.*, Responses of human cells to ZnO nanoparticles: A gene transcription study, *Metallomics*, 2011, **3**(11), 1199–1211.